Rare Metal Materials and Engineering
Volume 54, Issue 10, October 2025
Available online at www.rmme.ac.cn

Science Press

Cite this article as: Li Dianqi, Chai Yuanxin, Miao Liguo, et al. Temperature Prediction of Laser Directed Energy Deposition Based on ASSFOA-GRNN Model[J]. Rare Metal Materials and Engineering, 2025, 54(10): 2470-2482. DOI: https://doi.org/10.12442/j.issn.1002-185X.20240530.

ARTICLE

Temperature Prediction of Laser Directed Energy Deposition Based on ASSFOA-GRNN Model

Li Dianqi[1], Chai Yuanxin[1], Miao Liguo[1], Tang Jinghu[2]

[1] School of Mechanical Engineering, Shenyang University of Technology, Shenyang 110870, China; [2] School of Mechanical Engineering and Automation, Northeastern University, Shenyang 110819, China

Abstract: To address the issues of low accuracy, long time consumption, and high cost of the traditional temperature prediction methods for laser directed energy deposition (LDED), a machine learning model combined with numerical simulation was proposed to predict the temperature during LDED. A finite element (FE) thermal analysis model was established. The model's accuracy was verified through in-situ monitoring experiments, and a basic database for the predictive model was obtained based on FE simulations. Temperature prediction was performed using a generalized regression neural network (GRNN). To reduce dependence on human experience during GRNN parameter tuning and to enhance model prediction performance, an improved adaptive step-size fruit fly optimization algorithm (ASSFOA) was introduced. Finally, the prediction performance of ASSFOA-GRNN model was compared with that of back-propagation neural network model, GRNN model, and fruit fly optimization algorithm (FOA)-GRNN model. The evaluation metrics included the root mean square error (RMSE), mean absolute error (MAE), coefficient of determination (R^2), training time, and prediction time. Results show that the ASSFOA-GRNN model exhibits optimal performance regarding RMSE, MAE, and R^2 indexes. Although its prediction efficiency is slightly lower than that of the FOA-GRNN model, its prediction accuracy is significantly better than that of the other models. This proposed method can be used for temperature prediction in LDED process and also provide a reference for similar methods.

Key words: laser directed energy deposition; temperature prediction; FE simulation; generalized regression neural network; fruit fly optimization algorithm

1 Introduction

Laser directed energy deposition (LDED) technique uses high-energy laser beam to melt metal powder, and the powder stream is coaxial with the laser beam. As the heat source moves, the metal powder is rapidly melted and solidified, enabling deposition forming in point-by-point, line-by-line, and layer-by-layer manner[1–3]. LDED technique has several advantages, including high deposition efficiency, unlimited forming size, capability to prepare functional gradient materials, and the ability to repair and remanufacture critical components. Thus, LDED is widely used in various fields, such as aerospace, biomedicine, automotive, marine, and nuclear power. However, LDED is a high-energy processing technique, and the localized high-energy density heat input causes rapid heating and cooling of materials. This phenomenon generates an inhomogeneous temperature field, leading to significant residual stress, and potentially resulting in deformation, cracking, or even scrap of the part[4–6]. Therefore, accurately and efficiently predicting the temperature during LDED process is crucial.

With the rapid development of computer technology, numerical simulation has become a crucial tool to predict temperature evolution in the additive manufacturing process. Meng et al[7] developed a three-dimensional transient thermoelastic-plastic model for LDED process, which allows dynamic simulation of the temperature field with various process parameters and scanning strategies, achieving a simulation accuracy of approximately 82%. Dantin et al[8] created a finite-element (FE) model to predict the thermal

Received date: October 16, 2024
Foundation item: National Key Research and Development Program of China (2022YFB4602200)
Corresponding author: Chai Yuanxin, Ph. D., School of Mechanical Engineering, Shenyang University of Technology, Shenyang 110870, P. R. China, E-mail: chaiyuanxin@smail.sut.edu.cn

history of Ti-6Al-4V alloys and validated it through molten pool data collected by a dual-wavelength pyrometer. Pourabdollah et al[9] developed a three-dimensional transient thermodynamic model based on the layer aggregation method to rapidly predict the temperature in hollow rectangular parts during deposition. The prediction results were in good agreement with the measured data. Although these studies can predict the temperature during the forming process, they are only used in scientific research and are not suitable for industrial applications due to constraints related to computational cost, memory requirements, and the need for specialized expertise. With the rapid development of artificial intelligence technology, machine learning, which is well-known for its balance of computational cost and prediction capability, is gradually applied to temperature prediction in additive manufacturing processes. Zhou et al[10] proposed a 3D correction matrix based on a cubic mesh to describe the laser deposition state and used it as input for recurrent neural network (RNN)-deep neural network (DNN) model to predict the temperature field in gas metal arc welding, achieving a prediction accuracy of over 94%. However, because the size of the 3D input matrix determines the number of cells in the model, the actual size of additive manufacturing parts is restricted. Ren et al[11] established a thermal analysis model that combines RNN and DNN, achieving a prediction accuracy of over 95%. However, the model only applies to single-layer or single-track temperature field. Stathatos et al[12] proposed a custom-scanning path decomposition method and used artificial neural networks to predict the temperature evolution along arbitrarily long paths in laser additive manufacturing. Similarly, the model can only be validated for single-layer temperature fields. Zhu et al[13] developed a physically informed neural network model, which integrates data and physical principles to predict the temperature field in metallic additive manufacturing. This model achieves high prediction accuracy despite a limited training dataset. However, it does not account for the effects of free surface deformation and evaporation phenomena in the molten pool. Paul et al[14] developed a temperature prediction model based on an extremely random tree. This model takes previous voxel temperature and laser information as input and predicts the temperature of subsequent voxels with a mean absolute percentage error of less than 1%. However, as the feature set of the prediction model depends on neighboring voxels within a uniform mesh of rectangular elements, the geometric model must be simplified to generalize irregular geometries and meshes. Although machine learning methods offer new ways to predict the temperature in LDED, they are less effective in predicting temperature in short periods and require long training time as well as sophisticated analytical capabilities.

In this research, a method that combines machine learning with FE simulation was proposed to predict the temperature during LDED process. FE thermal analysis model was established and validated by in-situ temperature measurement experiments. Additionally, a database of machine learning models was created based on FE simulations. A generalized regression neural network (GRNN) was used to predict temperature with the optimal smoothing factor determined by an improved adaptive step-size fruit fly optimization algorithm (ASSFOA). Finally, the prediction performance of ASSFOA-GRNN model was compared with that of other machine learning models. The prediction model in this research provides reference for future studies to explore the effects of process parameters on the temperature field distribution of deposited parts, eliminating the need for complex FE analysis.

2 Experiment

The deposited material was Inconel 718 spherical powder prepared by the gas atomization method, whose particle size is 15–53 μm, and its chemical composition is shown in Table 1. Thin-walled parts with 20 mm in length and 6 mm in thickness were deposited onto Inconel 718 sheets with dimensions of 40 mm×40 mm×8 mm, and there were 20 layers in total. Before the experiment, the metal powder was dried to remove entrapped moisture and to improve its fluidity. The substrate surface was sanded to remove the oxide film and to enhance the absorption of the heat source. Finally, the substrate surface was cleaned with ethanol and dried to remove rust, oil, and dust. The temperature changes during the deposition process were drastic, and the thermo-physical property parameters of the material changed nonlinearly with the temperature. According to Ref. [15–17], the thermo-physical property parameters of Inconel 718 are shown in Fig.1.

The forming experiments were conducted using the Raycham LDM 4030 metal deposition system developed by Nanjing Zhongke Yuchen Laser Technology Co., Ltd. The laser has wavelength of 1070 nm and maximum output power of 2 kW, and argon was used as the protective gas. An aluminum oxide insulation board (80 mm×80 mm×6 mm) with excellent thermal insulation properties was placed between the substrate and the worktable. Temperature data at the test points on the substrate surface were recorded using type-K thermocouples (diameter of 1 mm) and TA612C multi-channel temperature data collector. The in-situ temperature measurement system is shown in Fig. 2. The measurement positions (T1 and T2) should be as close as possible to the heat source while maintaining a sufficient distance to avoid damage to the thermocouples.

3 Method

3.1 Thermal history dataset establishment

Numerous scholars have recognized that the main process parameters significantly impacting the temperature during deposition include laser power, scanning speed, and powder feeding rate[18–20]. Multiple levels were considered for each parameter, as shown in Table 2, and a total of 60 sets of

Table 1 Chemical composition of Inconel 718 (wt%)

Ni	Cr	Nb	Mo	Mn	Si	Al	Cu	Ti	C	Fe
51.71	18.93	5.12	3.08	0.13	0.14	0.49	0.05	0.97	0.04	Bal.

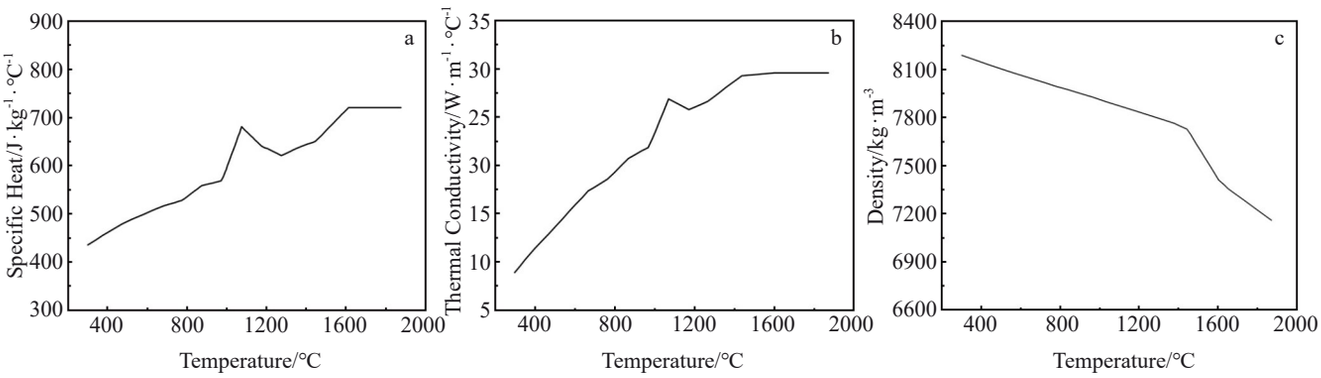

Fig.1 Thermo-physical property parameters of Inconel 718[15–17]: (a) specific heat, (b) thermal conductivity, and (c) density

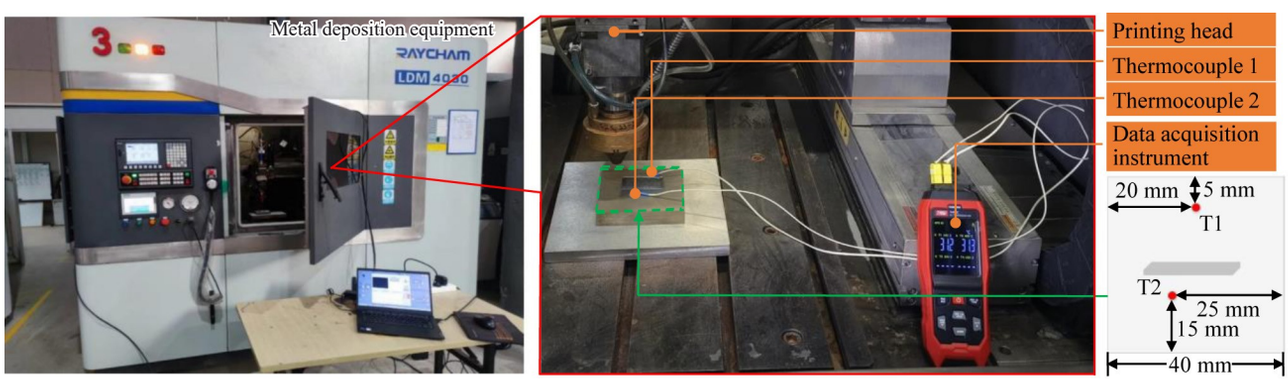

Fig.2 In-situ temperature measurement system

Table 2 Process parameters for thermal history dataset establishment

Process parameter	Value
Laser power, P/W	400, 500, 600, 700, 800
Scanning speed, v/mm·s^{-1}	6, 8, 10, 12
Powder feeding rate, f/g·s^{-1}	0.2, 0.3, 0.4
Laser spot diameter, d/mm	1.2
z-incremental height/mm	0.3

numerical simulations were performed. The dataset was divided with a ratio of 7:3, i.e., 42 sets of data for training and 18 sets for testing. The training and test datasets included the thermal history of all mesh points on the deposited track and the substrate.

This study used the thermodynamic coupling model developed in Ref. [21] to perform FE simulations, generating the thermal history dataset required for the machine learning model. The governing equation for nonlinear transient heat transfer in LDED process[22] is as follows:

$$\frac{\partial}{\partial x}\left(k_x\frac{\partial T}{\partial x}\right)+\frac{\partial}{\partial y}\left(k_y\frac{\partial T}{\partial y}\right)+\frac{\partial}{\partial z}\left(k_z\frac{\partial T}{\partial z}\right)+q=\rho c\frac{\partial T}{\partial t} \quad (1)$$

where k_x, k_y, and k_z are the thermal conductivities in the x, y, and z directions, respectively; q is the heat flux density; ρ is the material density; c is the specific heat of material; T is temperature.

FE analysis was conducted using a double ellipsoid heat source model, where the laser energy was distributed in a certain volume and applied to the nodes of the material model as heat flux density, as shown in Fig.3.

The heat flux density of the model along the front and rear semi-axes[23–24] of the ellipsoid is expressed by Eq. (2 – 3), respectively, as follows:

$$q_{\mathrm{f}}(x,y,z)=\frac{6\sqrt{3}\,f_{\mathrm{f}}Q}{\pi a_{\mathrm{f}}bc\sqrt{\pi}}\exp\left[-3\left(\frac{x^2}{a_{\mathrm{f}}^2}+\frac{y^2}{b^2}+\frac{z^2}{c^2}\right)\right] \quad (2)$$

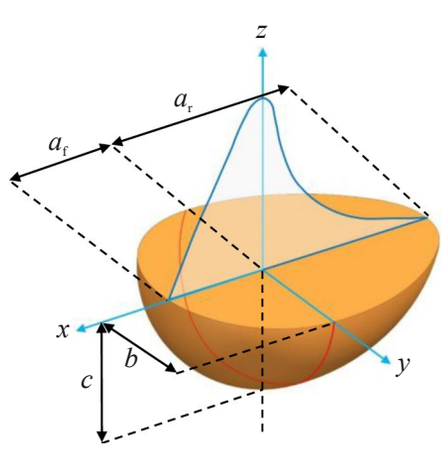

Fig.3 Schematic diagram of double ellipsoid heat source model

$$q_r(x,y,z)=\frac{6\sqrt{3}\,f_rQ}{\pi a_r bc\sqrt{\pi}}\exp\left[-3\left(\frac{x^2}{a_r^2}+\frac{y^2}{b^2}+\frac{z^2}{c^2}\right)\right] \quad (3)$$

where f_f and f_r are the heat flux distribution coefficients of the front and rear ellipsoids, respectively, and f_f+f_r=2; a_f and a_r are the lengths of the front and rear ellipsoids, respectively; b is the width of the heat source; c is the depth of the heat source; Q is the effective thermal power. Q can be expressed by Eq.(4), as follows:

$$Q=P\eta \quad (4)$$

where P is the laser power and η is the material absorption rate of laser energy.

The initial temperature condition during deposition is as follows:

$$T(x,y,z,t)|_{t=0}=T_0 \quad (5)$$

where t is time and T_0 is initial temperature.

The initial temperature of the metal powder and substrate is assumed to be 25 °C, according to the surrounding ambient air temperature.

The heat exchange during deposition is dominated by thermal convection and thermal radiation. The thermal boundary condition conforms to the third type of boundary condition[25]:

$$-k\frac{\partial T}{\partial n}=h_c(T-T_0)+\varphi\chi(T^4-T_0^4) \quad (6)$$

where k is the thermal conductivity, $\frac{\partial T}{\partial n}$ is the temperature gradient, h_c is the convective heat transfer coefficient, T is the surface temperature of the boundary of the object, T_0 is the temperature of the surrounding ambient medium, φ is the emissivity (ranging from 0 to 1), and χ is the Stefan-Boltzmann coefficient (approximately 5.67×10^{-8} W·m^{-2}·K^{-4}).

The birth-death element technique was employed to simulate the deposition process of the part. In order to balance computational efficiency and accuracy, a mesh convergence study was conducted[26–28]. A fine mesh with a minimum size of 1 mm was used in the deposition region and its neighboring areas, and the mesh was gradually coarsened with the increase in the distance from the deposition region. A total of 5238 cells and 7624 nodes were generated. The geometric meshing and scanning strategy of FE model are shown in Fig. 4. The scanning strategy employed the reciprocating paths with alternating scanning directions layer by layer.

Both the FE-based thermal simulations and the extraction of the dataset were performed on a workstation equipped with a 24-core processor (3.0 GHz) and 128 GB RAM. In machine learning, different features typically have different dimensions, directly affecting prediction performance. To mitigate the impact of varying feature dimensions, data normalization is necessary, as shown in Eq. (7), which maps the data to the range between 0 and 1[29]:

$$x_n=\frac{x_i-x_{min}}{x_{max}-x_{min}} \quad (7)$$

where x_n is the normalized data, x_i is the original data, x_{min} is the minimum value of the data, and x_{max} is the maximum value of the data.

3.2 Prediction model development

3.2.1 GRNN

GRNN is a highly parallel radial-basis neural network, and it was proposed in 1991. It has strong nonlinear mapping ability and fault tolerance, and it can better explain the complex nonlinear relationships between the predicted object and multiple influencing factors[30]. The model also performs better when the network data are sparse and can obtain optimized regression surfaces that converge with larger sample sizes and clustering. GRNN consists of a four-layer network, including an input layer, a pattern layer, a summation layer, and an output layer, as shown in Fig.5.

The essential functions of each layer in the network are as follows[31–33]:

(1) Input layer

The number of neurons in the input layer is determined by the dimensionality of the input data, and its role is to transmit the input data directly to the pattern layer.

(2) Pattern layer

The number of neurons in the pattern layer is the same as that in the input layer, and the transfer function is as follows:

$$P_i=\exp\left[-\frac{(X-X_i)^T(X-X_i)}{2\sigma^2}\right]\quad(i=1,2,\cdots,n) \quad (8)$$

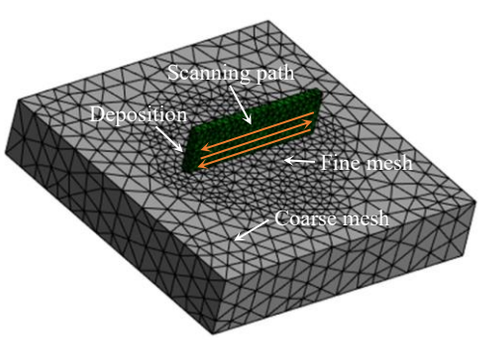

Fig.4 Schematic diagram of geometric meshing and scanning strategy

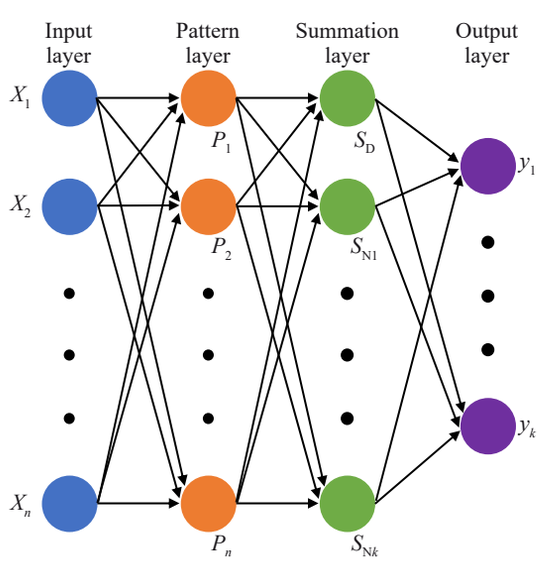

Fig.5 Schematic diagram of GRNN structure

where X represents the input parameter of the network, X_i denotes the learning sample corresponding to the ith neuron, and σ is the smoothing factor.

(3) Summation layer

The summation layer consists of two types of neurons. One type performs an arithmetic summation of the outputs from all the pattern layers. The transfer function for this type is denoted as follows:

$$S_{\mathrm{D}} = \sum_{i=1}^{n} P_i \tag{9}$$

The other type of neuron performs a weighted summation of the outputs from all the pattern layers. The transfer function for this type is expressed as follows:

$$S_{\mathrm{N}j} = \sum_{i=1}^{n} y_{ij} P_i \quad (j = 1, 2, \cdots, k) \tag{10}$$

where y_{ij} represents the weight between the ith neuron in the pattern layer and the jth neuron in the summation layer.

(4) Output layer

The number of neurons in the output layer equals the dimension value k of the output vector in the learning sample. Dividing the weighted summation output of the neurons in the summation layer by the arithmetic summation output gives the output of each neuron as follows:

$$y_j = \frac{S_{\mathrm{N}j}}{S_{\mathrm{D}}} \quad (j = 1, 2, \cdots, k) \tag{11}$$

GRNN determines its structure and connection weights based on the learning samples, and only the smoothing factor σ is adjustable. The model's predictive performance largely depends on the value of this smoothing factor σ[34]. As σ approaches 0, the predicted value tends to be the mean of all sample data, resulting in a significant prediction error. Conversely, as σ approaches infinity, the predicted value closely matches the training samples, which deteriorates the model's generalization ability and leads to overfitting, ultimately reducing prediction accuracy. The traditional method for determining the smoothing factor is often based on prior experience or through linear iteration. However, this approach is subjective, prone to randomness, and more likely to settle into a local optimum, significantly restricting the model's predictive capability[35]. To address this restriction, this study employs an intelligent optimization algorithm to ascertain the optimal smoothing factor for GRNN and to enhance its prediction performance.

3.2.2 ASSFOA

Fruit fly optimization algorithm (FOA) is an emerging swarm intelligence optimization method inspired by the foraging behavior of fruit fly populations. Compared to other swarm intelligence algorithms, FOA leverages fruit flies' unique olfactory and visual senses, offering advantages, such as simple implementation process, fewer parameters, strong searching capability, and rapid convergence. As a result, FOA has been widely applied in scientific research and practical engineering. Fig.6 illustrates the iterative evolutionary process of fruit fly populations. Based on the characteristics of the foraging behavior of fruit fly populations, FOA search process is as follows[36–38].

(1) Initialization of parameters. The parameters include population size (sizepop), maximum number of iterations (maxgen), and randomly initializing the position of the fruit fly population (X_{axis}, Y_{axis}).

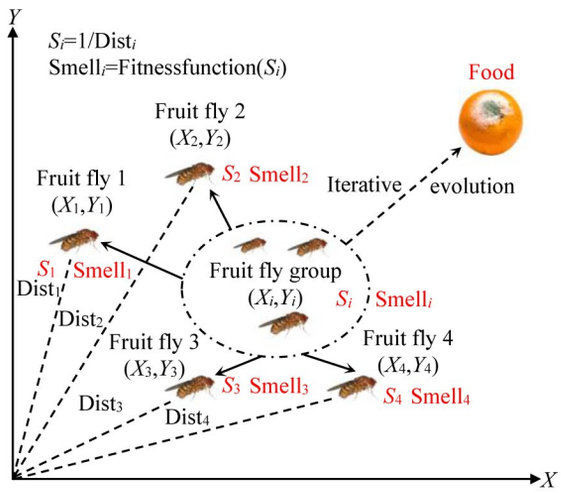

Fig.6 Iterative evolution procedure of FOA

(2) Olfactory search. When an individual fruit fly searches for food using its sense of smell, it is randomly assigned a direction and distance, and its position is updated, as follows:

$$\begin{cases} X_i = X_{\mathrm{axis}} + \mathrm{RandomValue} \\ Y_i = Y_{\mathrm{axis}} + \mathrm{RandomValue} \end{cases} \tag{12}$$

(3) Calculate the smell concentration judgment value. Since the exact position of the food cannot be determined initially, it is necessary to calculate the distance Dist_i between the current position of the fruit fly and the origin position. Then, compute the smell concentration judgment value S_i for each fruit fly.

$$\begin{cases} \mathrm{Dist}_i = \sqrt{X_i^2 + Y_i^2} \\ S_i = 1/\mathrm{Dist}_i \end{cases} \tag{13}$$

(4) Calculate the smell concentration value. Compute the smell concentration value Smell_i for each fruit fly by substituting the fruit fly's smell concentration judgment value S_i into the smell concentration judgment fitness function.

$$\mathrm{Smell}_i = \mathrm{Fitnessfunction}(S_i) \tag{14}$$

(5) Find the optimal individual. Identify the individual fruit fly with the best smell concentration value in the fruit fly population, and record its concentration and location.

$$[\mathrm{bestSmell},\ \mathrm{bestIndex}] = \min(\mathrm{Smell}) \tag{15}$$

(6) Visual localization. Record the fruit fly with the optimal smell concentration value in the current fruit fly population and its coordinates. If this smell concentration value is better, the fruit fly population will move to the new location.

$$\begin{cases} \mathrm{Smellbest} = \mathrm{bestSmell} \\ X_{\mathrm{axis}} = X(\mathrm{bestIndex}) \\ Y_{\mathrm{axis}} = Y(\mathrm{bestIndex}) \end{cases} \tag{16}$$

(7) Iterative optimization search. Repeat steps (2)–(5) to determine whether the optimal smell concentration value exceeds that of the previous generation until the number of iterations reaches the maximum value.

However, the standard FOA uses a fixed step size during its

iteration process. Increasing the step size enhances global search ability in the early stages and speeds up convergence. However, in the later stages of iteration, as the fruit fly population gets closer to the target, a larger step size can reduce local search ability, lower convergence accuracy, and may even cause the algorithm to oscillate around the neighborhood of the optimal solution without reaching it. If the step size is smaller, the local search ability of the fruit fly is enhanced, and convergence accuracy is improved. However, the convergence speed is slower in the early stages, which hinders global search and may cause the algorithm to fall into a local optimum. Therefore, this study used an adaptive step-size to balance global and local search abilities. The mutation and crossover operations from the differential evolution (DE) algorithm were incorporated into FOA, resulting in an improved algorithm: ASSFOA.

DE algorithm, proposed in 1995, is a stochastic heuristic search algorithm that simulates the "survival of the fittest" principle in natural biological populations. It has the advantages of simple principle, fast convergence, few controlled parameters, and strong robustness[39]. The basic principle of DE algorithm is as follows. Start with a randomly generated initial population of N_p individuals in a D-dimensional space. A mutation operation is firstly applied to selected individuals to generate mutant individuals. Next, a crossover operation is performed between the mutated individuals and the corresponding target individuals to create test individuals. Finally, based on the fitness of the test and target individuals, the best individuals are selected to form the next generation. Through continuous iterative optimization, DE algorithm systematically eliminates poorly adapted individuals while retaining the elite ones. This process ensures that the population gradually converges towards the global optimal solution. The three core steps of DE algorithm (mutation, crossover, and selection) are detailed below[40–42].

(1) Mutation operation

The mutation operation aims to transform each target individual in the parent population into a mutant individual. After evaluating several mutation strategies, the "DE/best/2" strategy is selected:

$$\boldsymbol{V}_i^g = \boldsymbol{X}_b^g + \boldsymbol{F} \times \left(\boldsymbol{X}_{r_1}^g - \boldsymbol{X}_{r_2}^g\right) + \boldsymbol{F} \times \left(\boldsymbol{X}_{r_3}^g - \boldsymbol{X}_{r_4}^g\right) \tag{17}$$

where $\boldsymbol{V}_i^g$ is the mutation vector; $\boldsymbol{X}_i^g$ is the target vector; $\boldsymbol{X}_b^g$ is the optimal individual obtained at the gth generation; $\boldsymbol{F}$ is a scaling factor, which controls the effect of the difference vector and takes values in the range [0, 1]; r_1, r_2, r_3, r_4, and r_5 are randomly selected integers from the range [1, N_P], distinct from each other and the index i, i.e., $r_1 \neq r_2 \neq r_3 \neq r_4 \neq r_5 \neq i$.

(2) Crossover operation

After generating the mutation vector $\boldsymbol{V}_i^g = \left(v_{i,1}^g, v_{i,2}^g, \cdots, v_{i,D}^g\right)$ corresponding to the target vector $\boldsymbol{X}_i^g = \left(x_{i,1}^g, x_{i,2}^g, \cdots, x_{i,D}^g\right)$, the test vector $\boldsymbol{U}_i^g = \left(u_{i,1}^g, u_{i,2}^g, \cdots, u_{i,D}^g\right)$ is generated through a crossover operation. The common crossover operation in differential evolution is the binomial crossover:

$$u_{i,j}^g = \begin{cases} v_{i,j}^g & \text{If rand} \leqslant C_R \text{ or } j = j_{\text{rand}} \\ x_{i,j}^g & \text{Otherwise} \end{cases} \tag{18}$$

where rand is a uniformly distributed random number in the interval [0, 1]; $C_R \in [0, 1]$ is the crossover probability; $j_{\text{rand}} \in [1, D]$ is a randomly selected dimension index, ensuring that at least one component of the test vector comes from the mutation vector.

(3) Selection operation

After generating the test vector through mutation and crossover operations, the fitness of the target vector and the test vector is compared using a selection operation. Consequently, the best individual is selected for the next generation to ensure that each iteration of the population evolution progresses toward the global optimum. The specific selection operation is detailed below:

$$\boldsymbol{X}_i^{g+1} = \begin{cases} \boldsymbol{U}_i^g & \text{If } f\left(\boldsymbol{U}_i^g\right) \leqslant f\left(\boldsymbol{X}_i^g\right) \\ \boldsymbol{X}_i^g & \text{Otherwise} \end{cases} \tag{19}$$

where $f(\boldsymbol{X})$ is the fitness of the individual vector $\boldsymbol{X}$.

In this study, the stochastic search step size of the standard FOA was updated using mutation and crossover operations. Meanwhile, the scaling factor was gradually decreased to enhance the optimization search capability of algorithm. The improvement strategy is as follows:

(1) Improved search step size

The search step size of the standard FOA is fixed. However, with the incorporation of the mutation operation from DE algorithm, the step size is dynamically updated based on the differences among population individuals, thereby enhancing the algorithm's capability to search for optima.

$$\begin{cases} \boldsymbol{U}_{x,j} = \boldsymbol{X}_{\text{axis}} + \boldsymbol{F} \times \left(\boldsymbol{X}_{r_1,j} - \boldsymbol{X}_{r_2,j}\right) + \boldsymbol{F} \times \left(\boldsymbol{X}_{r_3,j} - \boldsymbol{X}_{r_4,j}\right) \\ \boldsymbol{U}_{y,j} = \boldsymbol{Y}_{\text{axis}} + \boldsymbol{F} \times \left(\boldsymbol{Y}_{r_1,j} - \boldsymbol{Y}_{r_2,j}\right) + \boldsymbol{F} \times \left(\boldsymbol{Y}_{r_3,j} - \boldsymbol{Y}_{r_4,j}\right) \end{cases} \tag{20}$$

where r_1, r_2, r_3, and r_4 are random numbers within the interval [1, N_p], and N_p is the population size. To further increase the diversity of the population, the search step size continues to update using the crossover operation:

$$\text{RandomValue}_x = \begin{cases} \boldsymbol{U}_{x,j} & \text{If rand} \leqslant C_R \text{ or } j = j_{\text{rand}} \\ X_{\text{axis}} & \text{Otherwise} \end{cases} \tag{21}$$

$$\text{RandomValue}_y = \begin{cases} \boldsymbol{U}_{y,j} & \text{If rand} \leqslant C_R \text{ or } j = j_{\text{rand}} \\ Y_{\text{axis}} & \text{Otherwise} \end{cases} \tag{22}$$

(2) Improved scaling factor

In the early stages of iteration, when the population is far from the optimal solution, a larger search step size can enhance the algorithm's global search capability, allowing the fruit fly individuals to quickly reach the vicinity of the optimal solution. Once in the neighborhood of the optimal solution, the smaller search step size improves the algorithm's local search ability, enabling the optimal solution to be found more rapidly. Based on the abovementioned ideas, the scaling factor is improved to gradually decrease during the iteration process, thereby enhancing the algorithm's local search ability while ensuring the diversity of the population. The formula for the scaling

factor improvement is as follows:

$$F_{g+1} = F_g - \frac{F_0}{g_{\max}} \tag{23}$$

where g is the current iteration number, $g_{\max}$ is the maximum iteration number, and F_0 is the initial scaling factor.

3.2.3 Optimization of GRNN based on ASSFOA

The performance of GRNN is mainly affected by the smoothing factor σ. In this study, ASSFOA was employed to quickly optimize the smoothing factor of GRNN. The ASSFOA-GRNN model was used to predict the temperature during LDED process. The input variables include the coordinates (x, y, z) of the mesh points, laser power P, scanning speed v, and powder feeding rate f, while the predicted temperature T at the mesh points serves as the output variable. The prediction process of the ASSFOA-GRNN model mainly consists of two steps. (1) Internal parameter optimization: to ensure the validity and stability of the prediction model, the root mean square error (RMSE) between the predicted and actual values should be minimized, and the optimal smoothing factor for the GRNN is determined using ASSFOA. (2) External performance evaluation: the prediction model is constructed based on the determined optimal smoothing factor to predict the temperature during LDED process. The algorithm flow of the ASSFOA-GRNN model is illustrated in Fig.7.

$$\mathrm{RMSE} = \sqrt{\frac{1}{n}\sum_{i=1}^{n}\left(\hat{y}_i - y_i\right)^2} \tag{24}$$

where n is the total number of data samples, y_i is the actual value corresponding to the ith moment, and $\hat{y}_i$ is the predicted value corresponding to the ith moment.

4 Results and Discussion

4.1 Validation of thermal analysis of FE model

Before using simulated data to train the ASSFOA-GRNN model, the accuracy of FE model must be verified through actual deposition experiments. Ref.[21] has already validated the used FE model. To ensure the accuracy of the training data for the predictive model, a preliminary validation was conducted, though it is not analyzed in detail.

The temperature data from the test points on the surface of the substrate were measured using type-K thermocouples and compared with the results of FE simulation. The process parameters were set as follows: laser power of 600 W, scanning speed of 6 mm/s, powder feeding rate of 0.2 g/s, spot diameter of 1.2 mm, layer thickness of 0.3 mm, scanning strategy involving a reciprocating path with the scanning direction reversed layer by layer, and interlayer cooling for 5 s. The process parameters for the simulation and the experiment were consistent. The results of FE model are shown in Fig.8. The average errors between the simulated and

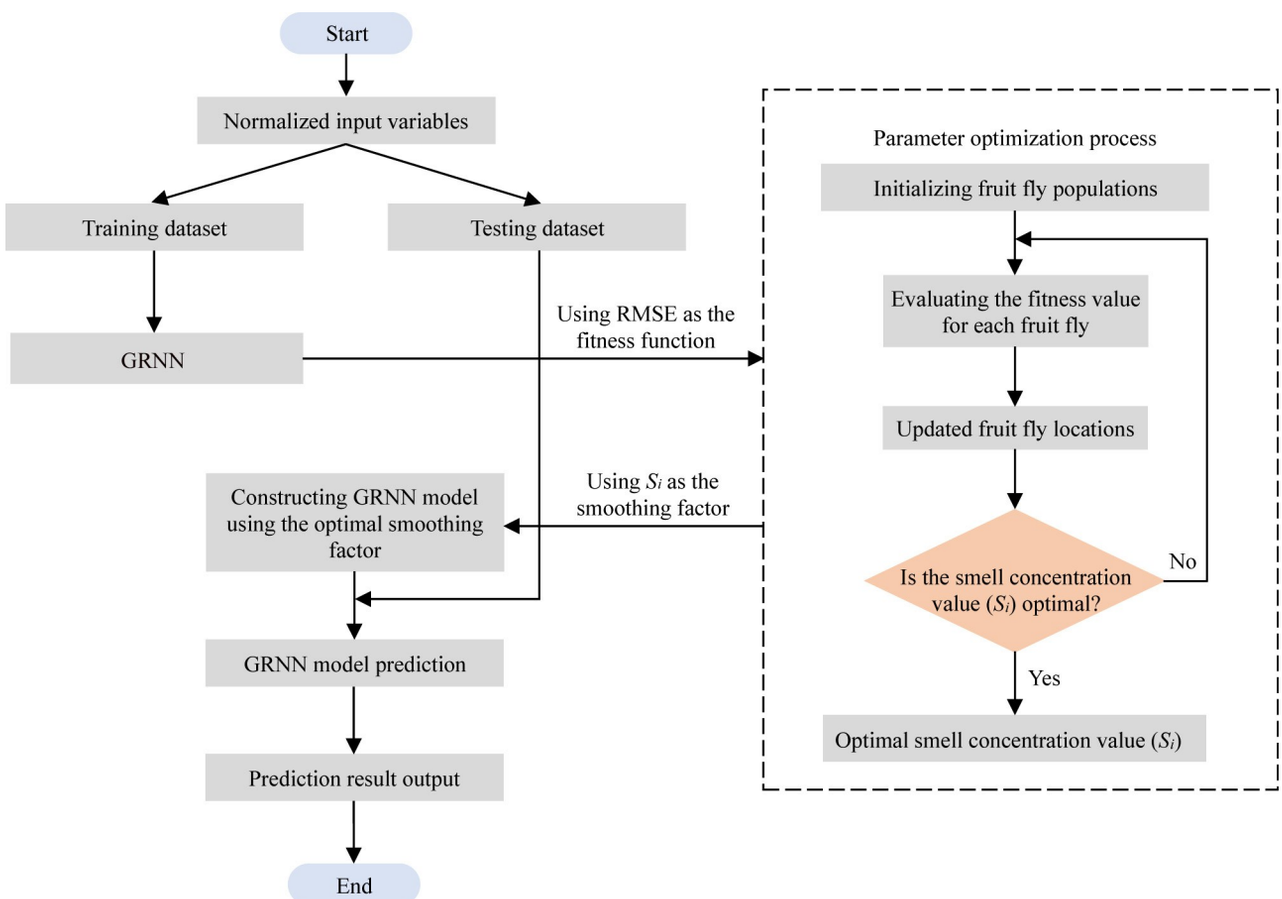

Fig.7 Flowchart of ASSFOA-GRNN

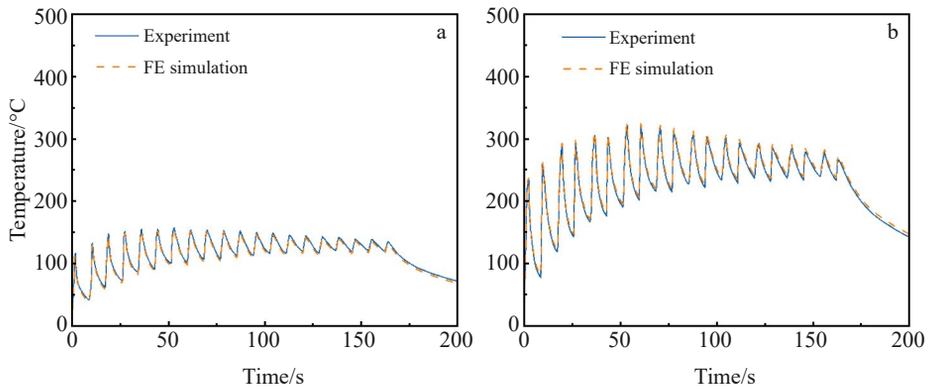

Fig.8 Comparison of temperatures at test point T1 (a) and test point T2 (b) obtained from FE simulation and experiment

measured temperatures at test points T1 and T2 are 4.48% and 3.15%, respectively. The simulated temperature profiles align well with the measured profiles, demonstrating the reliability of the thermal analysis of FE model in the prediction of temperature evolution during LDED process. The temperature profile simulated by FE model is highly consistent with the actual measured temperature profile, achieving an accuracy of 95.52%. Therefore, the data generated through FE simulation can be used as an essential dataset for constructing and training machine learning models.

4.2 Validation of machine learning model

ASSFOA-GRNN model proposed in this study was implemented into MATLAB 2019 with the relevant parameters as follows: crossover probability C_R=0.9, initial scaling factor F_0=0.9, fruit fly population size of 100, and maximum number of iterations of 1000. In order to validate the predictive performance of this machine learning model, the results of the ASSFOA-GRNN model and FE simulations were compared through the test dataset in two aspects: temperature-time distribution and temperature-spatial distribution. As shown in Table 3, 18 sets of randomly selected test data are presented.

In this study, RMSE, mean absolute error (MAE), and coefficient of determination (R^2) were used to assess the accuracy of temperature prediction by ASSFOA-GRNN model[43–45]. The closer the values of RMSE and MAE to 0, the more accurate the prediction results. Conversely, higher values of RMSE and MAE indicate less accurate predictions. Similarly, the closer the value of R^2 to 1, the better the model fitting result. Conversely, lower values of R^2 suggest an inferior model fitting.

$$\mathrm{MAE} = \frac{1}{n}\sum_{i=1}^{n}\left|\widehat{y_i} - y_i\right| \tag{25}$$

$$R^2 = 1 - \frac{\sum_{i=1}^{n}\left(y_i - \widehat{y_i}\right)^2}{\sum_{i=1}^{n}\left(y_i - \overline{y_i}\right)^2} \tag{26}$$

where n is the total number of data samples, y_i is the actual value of the ith element, $\widehat{y_i}$ is the predicted value corresponding to the ith element, and $\overline{y_i}$ is the predicted mean value corresponding to the ith element.

Table 3 Process parameters for test dataset

No.	Laser power, P/W	Scanning speed, v/mm·s^{-1}	Powder feeding rate, f/g·s^{-1}
1	400	6	0.4
2	400	8	0.2
3	400	10	0.3
4	500	6	0.4
5	500	8	0.3
6	500	10	0.2
7	500	12	0.4
8	600	6	0.2
9	600	8	0.4
10	600	10	0.3
11	600	12	0.4
12	700	8	0.3
13	700	10	0.4
14	700	12	0.2
15	800	6	0.3
16	800	8	0.2
17	800	10	0.4
18	800	12	0.3

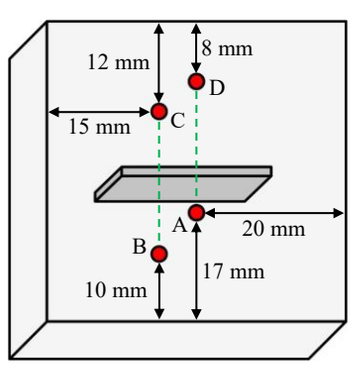

Fig.9 Test points for comparison of results predicted by ASSFOA-GRNN model and FE simulation

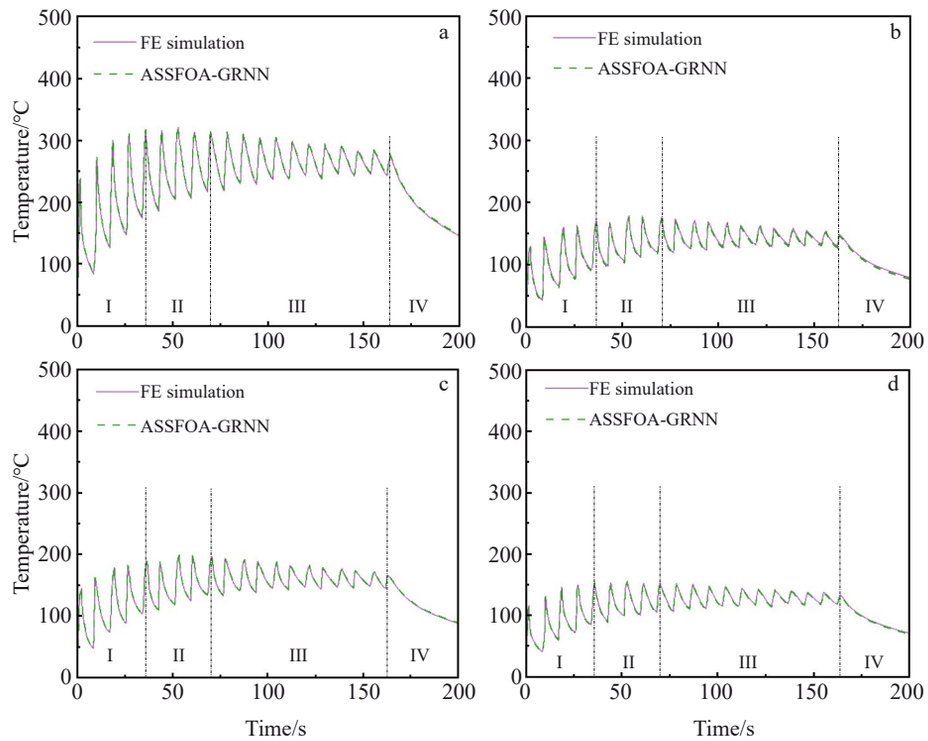

Fig.10 Comparison of temperatures at point A (a), point B (b), point C (c), and point D (d) predicted by FE simulation and ASSFOA-GRNN model under conditions of P=500 W, v=6 mm/s, and f=0.4 g/s

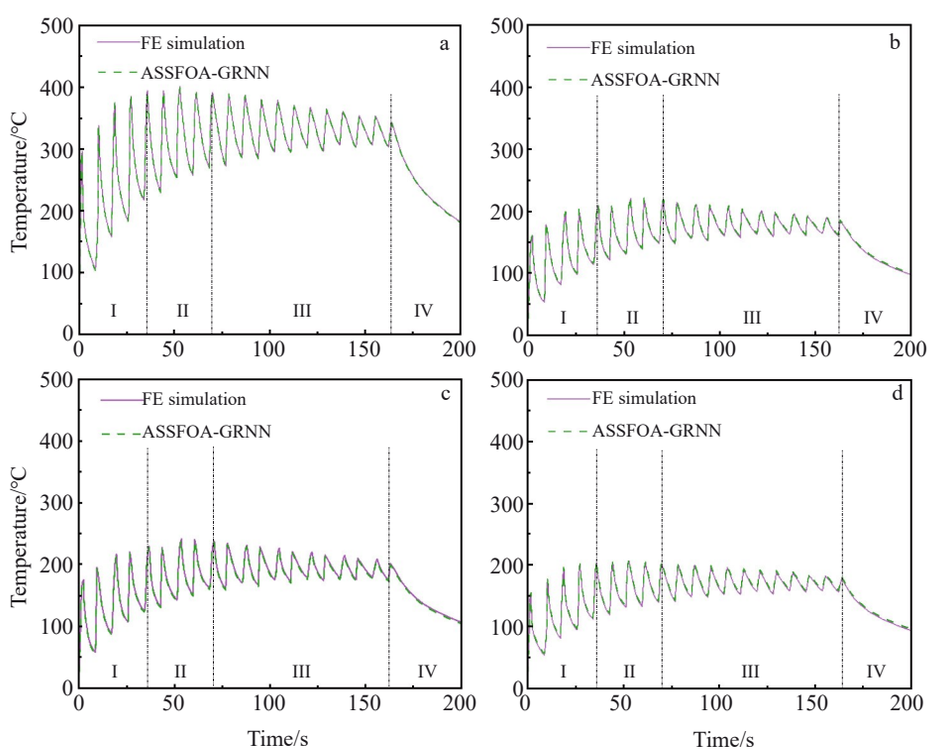

Fig.11 Comparison of temperatures at point A (a), point B (b), point C (c), and point D (d) predicted by FE simulation and ASSFOA-GRNN model under conditions of P=800 W, v=6 mm/s, and f=0.3 g/s

The locations of test points A, B, C, and D for verifying the temperature-time distribution results are shown in Fig. 9. Fig.10 and Fig.11 show the temperature profiles at points A to D under different working conditions, and ASSFOA-GRNN model results show high agreement with FE simulation results. The thermal response can be divided into four distinct

stages. In Stage I, the peak temperature increases as the number of deposited layers increases. In Stage II, the peak temperature gradually stabilizes. In Stage III, as the distance between the heat source and the substrate increases, the energy transferred from the laser to the substrate decreases, causing the peak temperature to decrease gradually. In Stage IV, after complete deposition, the temperature continues to decrease rapidly with the prolongation of cooling time. Similar thermal characteristics can be observed for other combinations of process parameters. Table 4 lists the predicted temperature-time distribution results for the test dataset. The R^2 values for each test point exceed 0.9970, while both the RMSE and MAE values are below 4 °C. These results all demonstrate that the ASSFOA-GRNN model not only captures the characteristics of the temperature profiles but also predicts the temperature-time distribution with high accuracy.

Fig. 12 shows the comparison of the representative temperature-spatial distributions predicted by FE simulation and ASSFOA-GRNN model at different deposition moments (t=50.95, 80.05 s) under No.8 condition (P=600 W, v=6 mm/s, and f=0.2 g/s). The ASSFOA-GRNN model demonstrates better agreement with the thermal contours generated by FE simulation. It can be observed that as the deposition proceeds, the heat accumulation effect becomes more pronounced, and the temperature of the molten pool continues to rise. When the deposition proceeds for 50.95 s, the peak temperature simulated by FE method is 1572.18 °C, while the peak temperature predicted by ASSFOA-GRNN model is 1573.62 °C, resulting in a difference of 1.44 °C. At 80.05 s, the peak temperature obtained from FE simulation is 1615.74 °C, while that predicted by ASSFOA-GRNN model is 1614.89 °C, and the difference is 0.85 °C. The high-temperature region is primarily concentrated in the deposition layers, which exhibit a large temperature gradient, whereas the temperature of the substrate farther from the upper deposition layers is lower and the temperature gradient is smaller. A similar phenomenon can be observed under process parameters. Table 5 lists the predicted temperature-spatial distribution results for the test dataset. The R^2 values under all conditions exceed 0.9975, while both the RMSE and MAE values are below 3 °C. These results indicate that the temperature fields simulated by FE model and those predicted by ASSFOA-GRNN model are in good agreement within an acceptable error range, and ASSFOA-GRNN model demonstrates high accuracy in predicting the temperature-spatial distribution.

The abovementioned examples of predictions based on temperature-time distribution and temperature-spatial distribution show that ASSFOA-GRNN model achieves a high level of accuracy in general. In summary, the temperature prediction method based on ASSFOA-GRNN model proposed in this study demonstrates the excellent feasibility of machine learning methods to predict the temperature during LDED process. For ASSFOA-GRNN model, the R^2 value is 0.9994, RMSE value is 2.58 °C, and MAE value is 1.94 °C.

4.3 Computational efficiency analysis of machine learning model

Table 6 shows the computational time of ASSFOA-GRNN model and FE simulation. To establish the training dataset, a total of 42 group FE simulations were conducted with each simulation duration of approximately 1.2 h. Thus, the total time required to establish the training dataset is approximately 50.4 h. The training time for ASSFOA-GRNN model is

Table 4 Prediction results of temperature-time distribution

No.	Point A			Point B			Point C			Point D		
	RMSE/°C	MAE/°C	R^2	RMSE/°C	MAE/°C	R^2	RMSE/°C	MAE/°C	R^2	RMSE/°C	MAE/°C	R^2
1	3.07	2.10	0.9972	1.58	1.27	0.9978	1.80	1.36	0.9986	2.14	1.67	0.9980
2	2.27	1.77	0.9991	2.84	2.18	0.9973	2.34	1.90	0.9979	3.34	2.26	0.9984
3	1.75	1.42	0.9983	2.67	1.98	0.9986	2.03	1.55	0.9974	1.66	1.34	0.9992
4	2.74	1.81	0.9971	3.55	2.73	0.9987	1.53	1.02	0.9978	2.19	1.57	0.9994
5	2.21	1.56	0.9988	1.61	1.17	0.9994	3.63	3.03	0.9981	1.96	1.44	0.9976
6	1.83	1.28	0.9982	3.11	2.12	0.9988	2.55	1.78	0.9993	1.92	1.38	0.9985
7	3.59	2.43	0.9989	2.30	1.74	0.9990	1.55	1.21	0.9971	3.18	2.16	0.9973
8	1.79	1.37	0.9993	1.64	1.26	0.9977	2.93	2.03	0.9990	2.46	1.68	0.9975
9	2.81	1.84	0.9974	1.87	1.32	0.9986	1.99	1.36	0.9989	2.97	1.98	0.9980
10	1.78	1.24	0.9980	2.90	2.04	0.9991	3.47	2.34	0.9975	3.60	2.32	0.9983
11	2.09	1.73	0.9995	1.88	1.50	0.9987	3.02	2.24	0.9992	2.42	1.88	0.9979
12	1.74	1.37	0.9977	3.76	2.47	0.9973	2.69	1.92	0.9984	1.95	1.46	0.9994
13	3.25	2.30	0.9989	2.16	1.62	0.9992	2.07	1.54	0.9976	2.38	1.72	0.9981
14	2.57	1.82	0.9978	3.71	3.04	0.9982	1.59	1.26	0.9989	2.72	1.99	0.9985
15	1.75	1.36	0.9991	2.78	2.05	0.9975	3.41	2.26	0.9983	3.23	2.59	0.9980
16	2.51	1.89	0.9977	1.68	1.38	0.9984	3.14	2.17	0.9990	2.23	1.77	0.9971
17	3.36	2.32	0.9981	2.89	2.16	0.9991	1.66	1.31	0.9978	1.71	1.29	0.9994
18	2.49	1.78	0.9988	3.82	3.15	0.9972	2.63	1.77	0.9992	1.88	1.49	0.9990

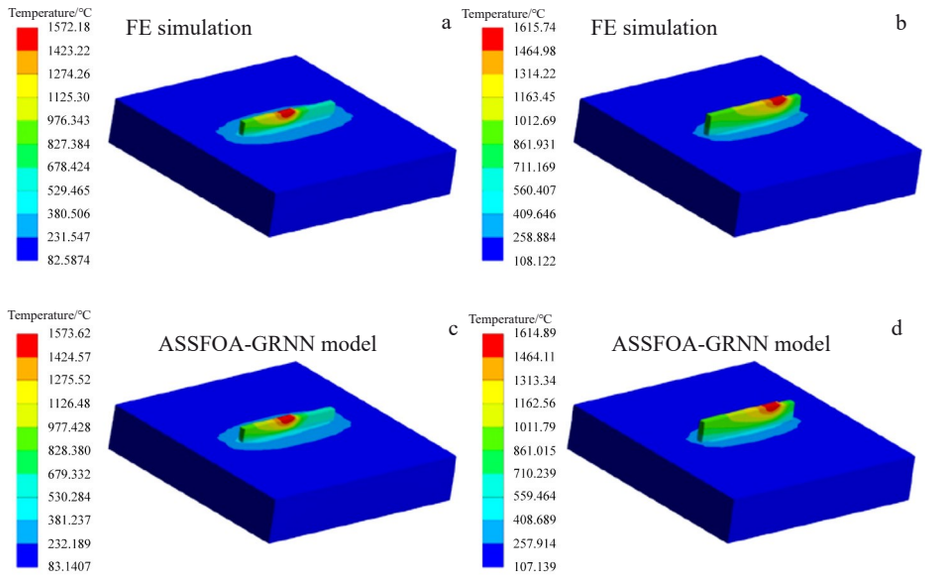

Fig.12 Comparison of temperature field distributions predicted by FE simulation (a–b) and ASSFOA-GRNN model (c–d) at deposition time of 50.95 s (a, c) and 80.05 s (b, d) under condition of P=600 W, v=6 mm/s, and f=0.2 g/s

Table 5 Prediction results of temperature-spatial distribution

No.	t=50.95 s			t=80.05 s		
	RMSE/°C	MAE/°C	R^2	RMSE/°C	MAE/°C	R^2
1	2.29	1.75	0.9990	1.73	1.36	0.9979
2	1.98	1.47	0.9982	1.86	1.40	0.9986
3	1.58	1.22	0.9977	2.96	2.18	0.9984
4	2.40	1.85	0.9980	2.58	2.08	0.9993
5	1.81	1.37	0.9979	2.06	1.63	0.9976
6	2.35	1.68	0.9978	1.79	1.34	0.9983
7	2.74	1.92	0.9995	1.90	1.56	0.9977
8	1.68	1.31	0.9988	2.84	2.04	0.9996
9	1.97	1.43	0.9992	2.77	2.13	0.9978
10	1.75	1.42	0.9983	1.40	1.02	0.9991
11	2.17	1.54	0.9978	2.66	1.96	0.9985
12	1.51	1.14	0.9989	2.55	1.99	0.9981
13	2.46	1.97	0.9993	1.37	1.06	0.9976
14	2.03	1.50	0.9977	2.31	1.83	0.9994
15	1.63	1.24	0.9990	1.84	1.36	0.9982
16	1.97	1.43	0.9987	1.35	1.04	0.9992
17	2.61	1.86	0.9989	1.49	1.12	0.9976
18	1.66	1.24	0.9978	2.24	1.61	0.9986

approximately 2.8 h. After training, the model can predict the temperature in only 10 s, greatly improving the computational efficiency by a factor of 432 compared to FE simulation. Since the training of the ASSFOA-GRNN model relies on the database established through FE simulations, ASSFOA-GRNN model does not show a significant advantage over FE simulations when making temperature predictions for small batches. However, when large batches of temperature fields for uncertainty quantification or process parameter optimization are required, the application of ASSFOA-GRNN model can significantly improve computational efficiency.

4.4 Comparison of predictive performance with other models

To further evaluate the prediction performance of ASSFOA-GRNN model, the prediction results of different machine learning models, including back-propagation neural network (BPNN) model, GRNN model, and FOA-GRNN model, were compared with those of ASSFOA-GRNN model on the test dataset. The parameters for all models were set to their optimal values. BPNN model is a multilayer feed-forward network model trained by the error back-propagation algorithm. Its network structure primarily consists of input, hidden, and output layers. The pertinent parameters of BPNN model are as follows. The maximum number of iterations was 5000, the learning rate was 0.01, the minimum error for the training objective was 0.000 01, and the number of hidden layers was 8. The smoothing factor of GRNN model was 0.1. The pertinent parameters for the FOA-GRNN model were as follows: the fruit fly population size was 100 and the maximum number of iterations was 2000.

Table 7 shows the comparison results of the predictive performance of different machine learning models. The

Table 6 Comparison of computational time between ASSFOA-GRNN model and FE simulation

Method	Time to establish the training dataset/h	Training time/h	Time to calculate a single temperature field
ASSFOA-GRNN model	50.4	2.8	10 s
FE simulation	-	-	1.2 h

Table 7 Comparison results of predictive performance of different machine learning models

Model	RMSE/ ℃	MAE/ ℃	R^2	Training time/h	Prediction time/s
ASSFOA-GRNN	2.58	1.94	0.9994	2.8	10
FOA-GRNN	13.61	9.83	0.9132	2.6	9
GRNN	22.93	16.15	0.8713	4.3	17
BPNN	38.47	29.86	0.6207	9.2	38

evaluation metrics for the models include RMSE, MAE, R^2, training time, and prediction time. It can be seen that the RMSE and MAE values of GRNN model are significantly smaller than those of BPNN model, and the R^2 is notably better. This indicates that the prediction accuracy of GRNN model is higher than that of BPNN model. This is because BPNN model uses the gradient descent method to update the weights, which can easily lead to local minima and prevent the model from finding the global optimal solution. Therefore, using GRNN model in this study for temperature prediction is reasonable. Compared with those of GRNN model, the RMSE and MAE values of FOA-GRNN model are reduced: RMSE decreases by 40.65% and MAE decreases by 39.13%. The R^2 value of FOA-GRNN model is slightly better than that of GRNN model and significantly better than that of BPNN model. This result indicates that although the unoptimized GRNN model has strong fitting ability, its predictive performance is restricted. Compared with that of FOA-GRNN, GRNN, and BPNN models, RMSE value of ASSFOA-GRNN model reduces by 81.04%, 88.75%, and 93.29%, respectively. Compared with that of FOA-GRNN, GRNN, and BPNN models, MAE value reduces by 80.26%, 87.99%, and 93.50%, respectively. Meanwhile, the R^2 increases by 9.44%, 14.70%, and 61.01%, compared with that of FOA-GRNN, GRNN, and BPNN models, respectively. These improvements all demonstrate that ASSFOA-GRNN model outperforms the other models in terms of prediction accuracy.

In addition to prediction accuracy, prediction efficiency is another critical metric for evaluating algorithms. The prediction efficiency of BPNN model is significantly lower than that of GRNN model. This is because GRNN model requires fewer parameters to be preset and eliminates the complex backpropagation process. The prediction efficiency of FOA-GRNN model is significantly improved compared with that of GRNN model because FOA can quickly find the optimal smoothing factor with fewer iterations. The slight decrease in prediction efficiency of ASSFOA-GRNN model, compared with that of the FOA-GRNN model, is due to the additional computational steps required by the mutation and crossover operations introduced in FOA, which increase the algorithm's computational complexity. Based on the abovementioned discussion, the ASSFOA-GRNN model achieves the optimal results in terms of RMSE, MAE, and R^2 metrics. Although its prediction efficiency is slightly lower than that of FOA-GRNN model, its prediction accuracy far exceeds that of the other models. Considering the trade-off between prediction accuracy and efficiency, ASSFOA-GRNN model demonstrates the optimal overall performance among these four temperature prediction models.

5 Conclusions

1) The temperature profile simulated by FE model is highly consistent with the actual measured temperature profile, achieving an accuracy of 95.52%. The model error is within an acceptable range. Consequently, the data generated by FE simulation can serve as a dataset for training machine learning models.

2) ASSFOA-GRNN temperature prediction model can accurately predict the temperature during LDED process, achieving very high accuracy. The R^2 value is 0.9994, RMSE value is 2.58 °C, and MAE value is 1.94 °C. The training time for the model is approximately 2.8 h, and only 10 s is required to make a quick temperature prediction after training.

3) ASSFOA-GRNN model is compared with BPNN, GRNN, and FOA-GRNN models. The results indicate that the ASSFOA-GRNN model achieves the highest prediction accuracy among all the compared models. In terms of prediction efficiency, the ASSFOA-GRNN model outperforms both the GRNN and BPNN models, though it is slightly less efficient than the FOA-GRNN model.

4) Overall, ASSFOA-GRNN model in this study performs excellently in temperature prediction. It not only significantly improves prediction efficiency while ensuring accuracy, but also demonstrates high practicality and application potential, making it highly significant for temperature prediction in LDED process.

References

1 Gao Jian, Liu Fencheng, Liu Fenggang *et al. Rare Metal Materials and Engineering*[J], 2023, 52(11): 3881 (in Chinese)

2 Das T, Mukherjee M, Chatterjee D *et al. CIRP Journal of Manufacturing Science and Technology*[J], 2023, 40: 114

3 Arrizubieta J I, Ostolaza M, Muro M *et al. International Journal of Heat and Mass Transfer*[J], 2023, 201: 123639

4 Kiran A, Hodek J, Vavřík J *et al. Materials*[J], 2020, 13(11): 2666

5 Ren K, Chew Y, Liu N *et al. Virtual and Physical Prototyping*[J], 2021, 16(3): 318

6 Cooke S, Sweet G, Ahmadi K *et al. Journal of Manufacturing Processes*[J], 2022, 81: 537

7 Meng G R, Zhang J D, Zhu L D *et al. Optics & Laser Technology*[J], 2023, 162: 109261

8 Dantin M J, Furr W M, Priddy M W. *Integrating Materials and Manufacturing Innovation*[J], 2022, 11(3): 407

9 Pourabdollah P, Farhang Mehr F, Maijer D M *et al. The International Journal of Advanced Manufacturing Technology*[J], 2023, 124(5): 1925

10 Zhou Z Y, Shen H Y, Liu B *et al. Journal of Manufacturing Processes*[J], 2021, 64: 960

11 Ren K, Chew Y, Zhang Y F *et al. Computer Methods in Applied Mechanics and Engineering*[J], 2020, 362: 112734
12 Stathatos E, Vosniakos G C. *The International Journal of Advanced Manufacturing Technology*[J], 2019, 104: 1967
13 Zhu Q M, Liu Z L, Yan J H. *Computational Mechanics*[J], 2021, 67: 619
14 Paul A, Mozaffar M, Yang Z *et al. 2019 IEEE International Conference on Data Science and Advanced Analytics* (*DSAA*)[C]. Washington: IEEE, 2019: 541
15 Chen Y, Guo Y B, Xu M J *et al. Materials Science and Engineering A*[J], 2019, 754: 339
16 Zhang J D, Meng G R, Zhu L D *et al. Applied Thermal Engineering*[J], 2022, 215: 118925
17 Polonsky A T, Raghavan N, Echlin M L P *et al. Materials Characterization*[J], 2022, 190: 112043
18 Xie Y P, Tong J B, Fu Y Q *et al. Journal of Mechanical Science and Technology*[J], 2020, 34: 3775
19 Khanafer K, Al-Masri A, Aithal S *et al. International Journal on Interactive Design and Manufacturing* (*IJIDeM*)[J], 2019, 13: 537
20 Sun F Z, Li Y, Fu Y X *et al. Optik*[J], 2020, 221: 165301
21 Chai Y X, Li D Q, Miao L G *et al. IEEE Access*[J], 2024, 12: 27723
22 Zeng G Z, Zu R L, Wu D L *et al. Experimental Mechanics*[J], 2021, 61: 1261
23 Wang J, Wang Y, Shi J. *International Journal of Precision Engineering and Manufacturing-Green Technology*[J], 2021, 8: 1181
24 Nain V, Engel T, Carin M *et al. Materials*[J], 2022, 15(12): 4093
25 Wang W, Ning J, Liang S Y. *International Journal of Precision Engineering and Manufacturing*[J], 2021, 22: 909
26 Lu X, Lin X, Chiumenti M *et al*. *Additive Manufacturing*[J], 2019, 26: 166
27 Lu X, Zhang G, Chiumenti M *et al*. *Virtual and Physical Prototyping*[J], 2023, 18(1): e2246041
28 Li B B, Gao E Z, Yin J *et al*. *Mathematics*[J], 2024, 12(6): 898
29 Pham T Q D, Hoang T V, Van Tran X *et al. Journal of Intelligent Manufacturing*[J], 2023, 34(4): 1701
30 Ruiming F, Shijie S. *Agricultural Water Management*[J], 2020, 236: 106177
31 Li B, Ding J Q, Yin Z Q *et al. Expert Systems with Applications*[J], 2021, 168: 114232
32 Li T, Shu J J, Chang D L. *Scientific Reports*[J], 2024, 14(1): 324
33 Shen C, Pei Z C, Chen W H *et al. IEEE Transactions on Instrumentation and Measurement*[J], 2023, 72: 2526614
34 Xu B X, Yi J X, Wan X R *et al. IEEE Sensors Journal*[J], 2023, 23(10): 10776
35 Niu D X, Wang H C, Chen H Y *et al. Energies*[J], 2017, 10(12): 2066
36 Lan C F, Li S J, Chen H *et al. Measurement*[J], 2021, 169: 108498
37 Fan Y, Wang P, Heidari A A *et al. Expert Systems with Applications*[J], 2020, 159: 113502
38 Fan Y, Wang P, Heidari A A *et al. Expert Systems with Applications*[J], 2020, 157: 113486
39 Zhao F, Wang C F, Liu H Q. *Complex & Intelligent Systems*[J], 2023, 9(5): 5033
40 Lin A P, Liu D, Li Z Q *et al. Complex & Intelligent Systems*[J], 2023, 9(6): 6905
41 Gupta S, Singh S, Su R *et al. IEEE/CAA Journal of Automatica Sinica*[J], 2023, 10(1): 135
42 Li Y Z, Wang S H, Yang B *et al. Artificial Intelligence Review*[J], 2023, 56(5): 3887
43 Xia C, Pan Z, Polden J *et al. Journal of Intelligent Manufacturing*[J], 2022, 33(5): 1467
44 Zhu X B, Jiang F C, Guo C H *et al. Optics & Laser Technology*[J], 2023, 159: 108964
45 Mbodj N G, Abuabiah M, Plapper P *et al. Applied Sciences*[J], 2021, 11(24): 11949

基于ASSFOA-GRNN模型的激光定向能量沉积温度预测

李殿起[1]，柴媛欣[1]，苗立国[1]，唐敬虎[2]

(1. 沈阳工业大学 机械工程学院，辽宁 沈阳 110870)

(2. 东北大学 机械工程与自动化学院，辽宁 沈阳 110819)

摘　要：针对传统的激光定向能量沉积（LDED）温度预测方法精度低、耗时长、成本高等问题，提出了一种结合数值模拟的机器学习模型来预测LDED过程中的温度。建立了有限元（FE）热分析模型，通过原位监测实验验证了模型的准确性，并基于FE模拟获得了预测模型的基础数据库。利用广义回归神经网络（GRNN）进行温度预测。为了减少GRNN调参过程中对人为经验的依赖并提升模型预测性能，引入了改进的自适应步长果蝇优化算法（ASSFOA）。最后将ASSFOA-GRNN模型与BPNN模型、GRNN模型和FOA-GRNN模型的预测性能进行了比较，评价指标包括均方根误差（RMSE）、平均绝对误差（MAE）、决定系数（R^2）、训练时间和预测时间。结果表明，ASSFOA-GRNN模型在RMSE、MAE和R^2指标上均表现最佳，尽管其预测效率略低于FOA-GRNN模型，但预测精度显著优于其他对比模型。本研究方法可用于LDED工艺的温度预测，也为同类方法的应用提供了借鉴。

关键词：激光定向能量沉积；温度预测；有限元模拟；广义回归神经网络；果蝇优化算法

作者简介：李殿起，男，1968年生，博士，教授，沈阳工业大学机械工程学院，辽宁 沈阳 110870，E-mail：dianqi@126.com